Since January 2020 Elsevier has created a COVID-19 resource centre with free information in English and Mandarin on the novel coronavirus COVID-19. The COVID-19 resource centre is hosted on Elsevier Connect, the company's public news and information website.

Short Article

Cell Host & Microbe

Evasion of neutralizing antibody responses by the SARS-CoV-2 BA.2.75 variant

Highlights

- BA.2.75 shows enhanced neutralization resistance and fusion over BA.2 but not BA.4/5
- G446S, and to a lesser extent N460K, determines enhanced neutralization resistance
- N460K drives enhanced spike processing and cell-cell fusion of BA.2.75
- N460K potentiates ACE2 interactions likely by forming a salt bridge and hydrogen bond

Authors

Panke Qu, John P. Evans, Yi-Min Zheng, ..., Kai Xu, Richard J. Gumina, Shan-Lu Liu

Correspondence

liu.6244@osu.edu

In brief

Newly emerged Omicron subvariants reignite concerns over escape from existing immunity. Qu and colleagues compare the immunity resistance and fusogenicity of BA.2.75 with prior variants. BA.2.75 exhibits stronger neutralization resistance than BA.2 but weaker than BA.4/5, as well as enhanced fusogenicity, which are largely driven by G446S and N460K, respectively.

Qu et al., 2022, Cell Host & Microbe *30*, 1518–1526
November 9, 2022
https://doi.org/10.1016/j.chom.2022.09.015

CellPress

CellPress

Cell Host & Microbe

Short Article

Evasion of neutralizing antibody responses by the SARS-CoV-2 BA.2.75 variant

Panke Qu,[1,2,11] John P. Evans,[1,2,3,11] Yi-Min Zheng,[1,2] Claire Carlin,[4] Linda J. Saif,[5,6,7] Eugene M. Oltz,[8] Kai Xu,[1,2] Richard J. Gumina,[4,9,10] and Shan-Lu Liu[1,2,7,8,12,*]

[1]Center for Retrovirus Research, The Ohio State University, Columbus, OH 43210, USA
[2]Department of Veterinary Biosciences, The Ohio State University, Columbus, OH 43210, USA
[3]Molecular, Cellular, and Developmental Biology Program, The Ohio State University, Columbus, OH 43210, USA
[4]Department of Internal Medicine, Division of Cardiovascular Medicine, The Ohio State University, Columbus, OH 43210, USA
[5]Center for Food Animal Health, Animal Sciences Department, OARDC, College of Food, Agricultural and Environmental Sciences, The Ohio State University, Wooster, OH 44691, USA
[6]Veterinary Preventive Medicine Department, College of Veterinary Medicine, The Ohio State University, Wooster, OH 44691, USA
[7]Viruses and Emerging Pathogens Program, Infectious Diseases Institute, The Ohio State University, Columbus, OH 43210, USA
[8]Department of Microbial Infection and Immunity, The Ohio State University, Columbus, OH 43210, USA
[9]Dorothy M. Davis Heart and Lung Research Institute, The Ohio State University Wexner Medical Center, Columbus, OH 43210, USA
[10]Department of Physiology and Cell Biology, College of Medicine, The Ohio State University Wexner Medical Center, Columbus, OH 43210, USA
[11]These authors contributed equally
[12]Lead contact
*Correspondence: liu.6244@osu.edu
https://doi.org/10.1016/j.chom.2022.09.015

SUMMARY

The newly emerged BA.2.75 severe acute respiratory syndrome coronavirus 2 (SARS-CoV-2) variant contains 9 additional mutations in its spike (S) protein compared to the ancestral BA.2 variant. Here, we examine the neutralizing antibody escape of BA.2.75 in mRNA-vaccinated and BA.1-infected individuals, as well as the molecular basis underlying functional changes in S. Notably, BA.2.75 exhibits enhanced neutralization resistance over BA.2 but less than the BA.4/5 variant. The G446S and N460K mutations of BA.2.75 are primarily responsible for its enhanced resistance to neutralizing antibodies. The R493Q mutation, a reversion to the prototype sequence, reduces BA.2.75 neutralization resistance. The impact of these mutations is consistent with their locations in common neutralizing antibody epitopes. Further, BA.2.75 shows enhanced cell-cell fusion over BA.2, driven largely by the N460K mutation, which enhances S processing. Structural modeling reveals enhanced receptor contacts introduced by N460K, suggesting a mechanism of potentiated receptor utilization and syncytia formation.

INTRODUCTION

Emergence of the Omicron variant of severe acute respiratory syndrome coronavirus 2 (SARS-CoV-2) in late 2021 sparked an unprecedented wave of coronavirus disease 2019 (COVID-19) cases and exhibited robust evasion of vaccine- and infection-induced immunity (Gruell et al., 2022; Hoffmann et al., 2022). More recently, several subvariants of Omicron have been identified, which have driven subsequent waves of infection. The BA.1 subvariant, responsible for the initial Omicron wave, was replaced by BA.2, which displayed slightly enhanced transmissibility and resistance to BA.1-induced sera (Evans et al., 2022; Yamasoba et al., 2022b). BA.2 then evolved into several progeny subvariants, including the BA.2.12.1 variant, which subsequently became predominant (Centers for Disease Control and Prevention, 2022). Remarkably, the BA.4 and BA.5 variants, which bear identical spike (S) proteins and evolved from BA.2, are currently dominant worldwide, including in the US (Centers for Disease Control and Prevention, 2022). BA.4 and BA.5 bear an L452R mutation that is primarily responsible for further enhanced neutralizing antibody (nAb) resistance (Qu et al., 2022a; Qu et al., 2022b; Tuekprakhon et al., 2022). Recently, another distinct BA.2-derived subvariant, BA.2.75, has been identified. BA.2.75 is increasing in prevalence in southeast Asia and has been detected globally (Callaway, 2022). Notably, BA.2.75 bears 9 key S mutations including K147E, W152R, F157L, I210V, G257S, D339H, G446S, and N460K, as well as an R493Q reversion mutation (World Health Organization, 2022) (Figure 1A). These mutations, particularly those in the receptor binding domain (RBD), have generated concern over further immune escape.

Here we characterize the BA.2.75 S protein by examining its sensitivity to neutralizing antibodies from mRNA-vaccinated and/or boosted health care workers (HCWs), as well as from Omicron-wave-hospitalized COVID-19 patients. In addition, we examine BA.2.75 infectivity, S processing, and fusogenicity. Mutational analysis revealed the N460K as a key driver of

CellPress

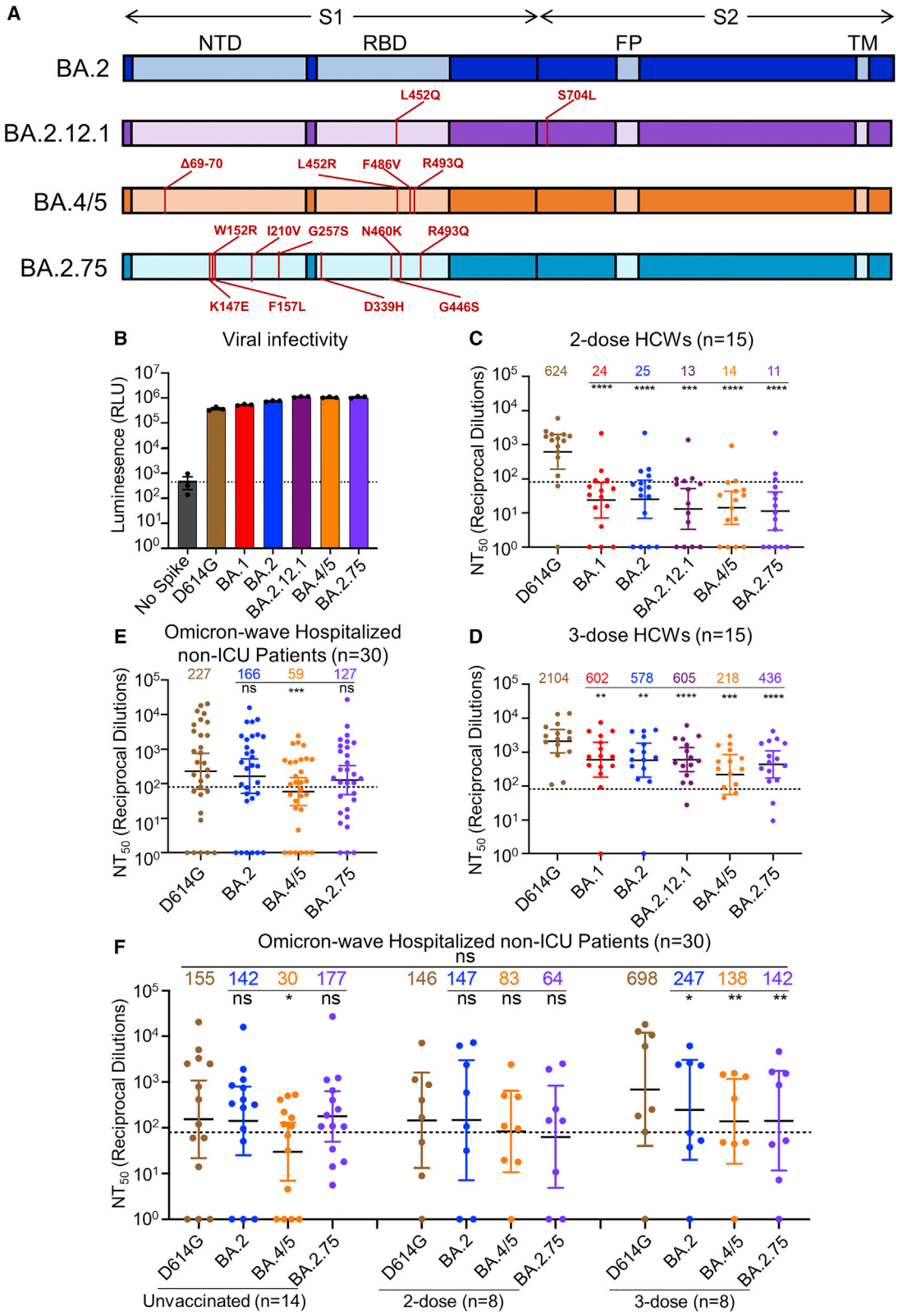

Figure 1. BA.2.75 exhibits strong neutralization resistance to 2-dose and 3-dose mRNA vaccinee sera and Omicron-wave patient sera

(A) Schematic of BA.2-derived SARS-CoV-2 variants with mutations relative to the BA.2 background indicated. Highlighted are the S1 and S2 subunits, N-terminal domain (NTD), receptor binding domain (RBD), fusion peptide (FP), and transmembrane (TM) domain.

(legend continued on next page)

enhanced fusogenicity, while the G446S and N460K mutations were primarily responsible for reduced neutralization sensitivity of BA.2.75 compared to BA.2. Moreover, we find that the R493Q reversion mutation enhances the neutralization sensitivity of BA.2.75. These findings inform our understanding of SARS-CoV-2 evolution and will aid in addressing the ongoing threat of emerging SARS-CoV-2 variants.

RESULTS

BA.2.75 exhibits enhanced neutralization resistance over BA.2

We first sought to characterize sensitivity to vaccine-induced immunity of the BA.2.75 variant. Utilizing our previously reported pseudotyped lentivirus assay (Zeng et al., 2020), we examined nAb titers for 15 Ohio State University Wexner Medical Center HCWs in serum samples collected 3–4 weeks after vaccination with a second dose of Moderna mRNA-1273 (n = 7) or Pfizer/BioNTech BNT162b2 (n = 8) vaccine, and 1–12 weeks after vaccination with a homologous booster dose (see STAR Methods). Patient sera were examined for nAb titers against lentivirus pseudotyped with S from ancestral SARS-CoV-2 S bearing only the D614G mutation, as well as S from BA.1, BA.2, BA.2.12.1, BA.4/5, and BA.2.75 (Figure 1A). All S constructs were functional and produced comparably infectious lentivirus pseudotypes (Figure 1B).

Notably, all Omicron sublineages, including BA.2.75, exhibited strong resistance to 2-dose-induced immunity compared to D614G ($p < 0.0001$), with only 1–2 HCW samples exhibiting 50% neutralization titers (NT_{50}) above the limit of quantification ($NT_{50} = 80$) (Figure 1C). In contrast, administration of a booster dose recovered the nAb response against all Omicron subvariants (Figures 1D and S1A–S1H). In serum from the boosted individuals, BA.2.75 exhibited 4.8-fold ($p < 0.0001$) lower neutralization than D614G, with somewhat stronger neutralization resistance than BA.2 and BA.2.12.1, which were neutralized 3.6-fold ($p < 0.01$) and 3.5-fold ($p < 0.001$) less efficiently than D614G, respectively (Figure 1D). However, BA.2.75 showed higher neutralization sensitivity than BA.4/5, which had 9.7-fold ($p < 0.001$) lower neutralization than D614G (Figure 1D).

We also examined the nAb response in a cohort of non-intensive care unit (ICU) COVID-19 patients (n = 30) hospitalized at the Ohio State University Wexner Medical Center during the Omicron wave of the pandemic. These patient samples were collected between early February and early March of 2022, representing a BA.1 dominant period in Ohio. Overall, the nAb titers of the Omicron-wave patients were much lower than those of boosted HCWs, and BA.2.75 exhibited neutralization resistance modestly higher than BA.2 (by 44.0%, $p > 0.05$) but much lower than BA.4/5 (3.8-fold; $p < 0.001$) relative to D614G (Figures 1E and S1I). This cohort of Omicron-wave patients included 14 unvaccinated patients, 8 patients vaccinated with 2 doses of Moderna mRNA-1273 (n = 4) or Pfizer/BioNTech BNT162b2 (n = 4), and 8 patients vaccinated and boosted with Pfizer/BioNTech BNT162b2. We found that, while BA.2.75 was neutralized comparably to BA.2 and D614G for unvaccinated patients, BA.2.75 was neutralized 2.3-fold less efficiently than D614G in 2-dose vaccinated patients ($p > 0.05$) and 4.9-fold less efficiently for 3-dose vaccinated patients ($p < 0.01$), respectively (Figure 1F). The boosted HCWs with breakthrough infection exhibited higher nAb titers overall (Figure 1F), as would be expected.

BA.2.75 neutralization is modulated by G446S, N460K, and R493Q mutations

To understand the determinants of BA.2.75 neutralization resistance, we examined all nine point mutations in the BA.2 background, as well as nine corresponding reversion mutations in the background of BA.2.75. None of these single mutations substantially impacted lentiviral pseudotype infectivity (Figures 2A and 2B). We then examined the neutralization sensitivity of these mutants to sera from 9 HCWs collected 1–12 weeks after homologous booster vaccination with Moderna mRNA-1273 (n = 2) or Pfizer/BioNTech BNT162b2 (n = 7). When the G446S mutation was introduced to BA.2, a slight but significant reduction in sensitivity to 3-dose mRNA vaccine-induced nAbs was observed (42.7%, $p < 0.01$), which was comparable to BA.2.75 (Figure 2C). Introduction of a S446G reversion mutation into BA.2.75 enhanced neutralization sensitivity by 31.4%, albeit the change was not statistically significant ($p = 0.055$) (Figure 2D). Interestingly, introduction of a R493Q mutation into BA.2 increased neutralization sensitivity by 35.8% ($p > 0.05$), while introduction of the Q493R reversion mutation into BA.2.75 reduced neutralization sensitivity by 45.1% ($p > 0.05$) (Figures 2C and 2D). Of note, the N460K mutation also substantially increased neutralization resistance of BA.2 by 33.0% ($p > 0.05$), whereas the K460N reversion mutation in BA.2.75 was 77.4% ($p = 0.069$) more neutralization sensitive (Figures 2C and 2D). Thus, the G446S and N460K mutations in BA.2.75 are largely responsible for its enhanced neutralization resistance, while the R493Q reversion mutation in BA.2.75 at least partially restores neutralizing epitopes found in the prototype SARS-CoV-2, which were otherwise abolished in BA.2.

BA.2.75 exhibits enhanced syncytia formation and S processing compared to BA.2

We next sought to characterize key features of the BA.2.75 S protein, including the ability to mediate cell-cell fusion. HEK293T cells stably expressing human angiotensin I converting enzyme 2 (ACE2) (HEK293T-ACE2 cells) were transfected to

(B) Infectivity of pseudotyped lentivirus bearing S protein from SARS-CoV-2 variants of study; bars represent means ± standard error.
(C and D) Neutralizing antibody titers against lentivirus pseudotyped with S from individual SARS-CoV-2 variants for 15 health care workers for sera collected 3–4 weeks after second mRNA vaccination (C) or 1–12 weeks after homologous mRNA booster vaccination (D).
(E) Neutralizing antibody titers for sera collected from 30 COVID-19 patients hospitalized during the BA.1 pandemic wave.
(F) Neutralizing antibody titers against hospitalized BA.1 wave patients are divided by vaccination status.
(C–F) Dots indicate individual patient samples; bars represent geometric means with 95% confidence intervals; significance relative to D614G was determined by one-way repeated measures ANOVA with Bonferroni multiplicity correction. p values are displayed as *$p < 0.05$, **$p < 0.01$, ***$p < 0.001$, ****$p < 0.0001$, and ns for not significant.

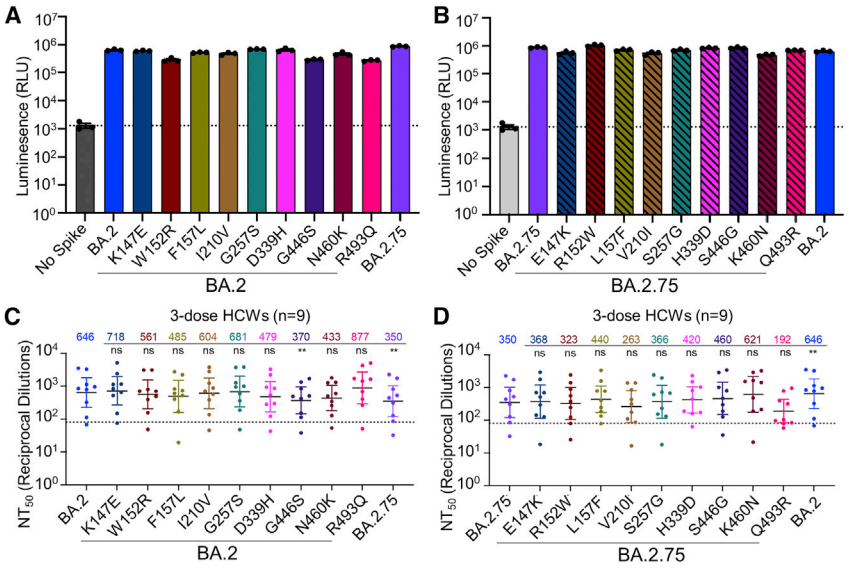

Figure 2. The G446S, N460K, and R493Q mutations modulate BA.2.75 neutralization sensitivity

(A) Relative infectivity of lentivirus pseudotyped with BA.2 S with single mutations from BA.2.75 lineage-defining mutations; bars represent mean ± standard error.

(B) Relative infectivity of lentivirus pseudotyped with BA.2.75 S with single reversion mutations to remove BA.2.75 lineage-defining mutations; bars represent mean ± standard error.

(C and D) Neutralizing antibody titers against lentivirus pseudotyped with S from BA.2 with single mutations from BA.2.75 lineage-defining mutations (C) or BA.2.75 with single reversion mutations to remove BA.2.75 lineage-defining mutations (D) for sera collected from 9 health care workers 1–12 weeks after homologous mRNA booster vaccination. Dots indicate individual patient samples; bars represent geometric means with 95% confidence intervals; significance relative to D614G was determined by one-way repeated measures ANOVA with Bonferroni multiplicity correction. p values are displayed as $^{**}p < 0.01$, and ns for not significant.

express the green fluorescent protein (GFP) and variant SARS-CoV-2 S proteins. As previously reported (Zeng et al., 2021), all Omicron sublineages exhibited reduced fusogenicity compared to the ancestral D614G S (Figures 3A and 3B). However, BA.2.75 exhibited enhanced syncytia formation compared to BA.2, with mean syncytia size 2.0-fold higher than BA.2 ($p < 0.0001$) (Figures 3A, 3B, and S2A); this was despite similar surface expression, as examined by flow cytometry (Figures 3C and 3D).

To determine if the enhanced fusogencity phenotype might be related to alterations in processing of S protein, we examined cell lysates from the pseudotyped lentivirus producer cells. As shown in Figure 3E, BA.2.75 spike exhibited enhanced processing, as reflected in the ratio of S1 or S2 subunit to full-length S, which was ~30%–40% higher than BA.2. Consistent with its enhanced fusion, BA.4/5 showed the highest S processing among Omicron variants (Figures 3A, 3B, 3E, and S2A).

Enhanced syncytia formation and processing of BA.2.75 is determined by the N460K mutation

We further characterized the impact of BA.2.75-defining mutations on S fusogenicity and processing. Introduction of the N460K mutation into the BA.2 S drastically enhanced cell-cell fusion, with mean syncytia size 3.8-fold ($p < 0.0001$) higher than BA.2 (Figures 4A, 4B, and S2B). Conversely, introduction of the K460N reversion mutation into BA.2.75 significantly reduced cell-cell fusion, with mean syncytia size 4.3-fold ($p < 0.0001$) lower than BA.2.75 (Figures 4C, 4D, and S2C). We found that F157L and G257S in the BA.2 background, as well as the R152W reversion mutant in the BA.2.75 background, also exhibited modestly altered fusion activity (Figures 4A–4D). Importantly, the differences in membrane fusion between these mutants were not due to the surface expression level of S, as examined by flow cytometry (Figures 4E, 4F S2D, and S2E). Consistent with enhanced fusion activity, introduction of the N460K mutation into the BA.2 S protein enhanced processing of S into the S1 and S2 subunits, as reflected in a S1/S ratio 40% higher than in BA.2 (Figure 4G); a similar 70% increase in S2/S ratio was also observed (Figure 4G). Conversely, introduction of a K460N reversion mutation into BA.2.75 reduced S protein processing by 20% (Figure 4H). Thus, the N460K mutation in BA.2.75 enhances S processing, consistent with increased fusogenicity.

Structural modeling

To understand how BA.2.75 mutations contribute to functional changes, we created models of ectodomain of BA.2.75 by itself, as well as ectodomain or RBD of BA.2.75 spike protein in complexes with the ACE2 receptor using homology modeling using Omicron BA.1 spike and its ACE2 complex (PDB: 7TNW and 7TO4) and BA.2 RBD-ACE2 complex (PDB: 7XB0) as templates (Figures 4I and S3). The G446S mutation does not appear to alter main-chain interactions with the Q42 receptor residue; however, this mutation could reduce backbone flexibility, thus potentially stabilizing the specific interaction with ACE2, as well as spike integrity. The R493Q mutation would abolish a strong salt bridge interaction with the E35 residue on the ACE2 receptor, which could reduce receptor binding affinity; however, this effect may be offset by the formation of two new hydrogen bonds between the Q493 residue on spike and residues E35 and K31 on ACE2. Finally, N460K forms a new hydrogen bond with the glycan-N90 on ACE2 through an elongated side chain that reaches out to the alpha-1,3 mannose molecule on the N-linked glycan of the receptor residue N90, and this would likely enhance receptor binding affinity of BA.2.75. In addition, N460K could form a salt bridge with D240 (Cao et al., 2022) and hydrogen bond with T415 on RBD, respectively, which would enhance intra-RBD hydrophilic interactions, resulting in reduced flexibility of ACE2-contacting loops on the receptor binding motif (RBM) therefore facilitating receptor engagement.

DISCUSSION

The BA.2.75 subvariant is the latest in a series of Omicron variants to be identified. BA.2.75 has an alarming nine additional S

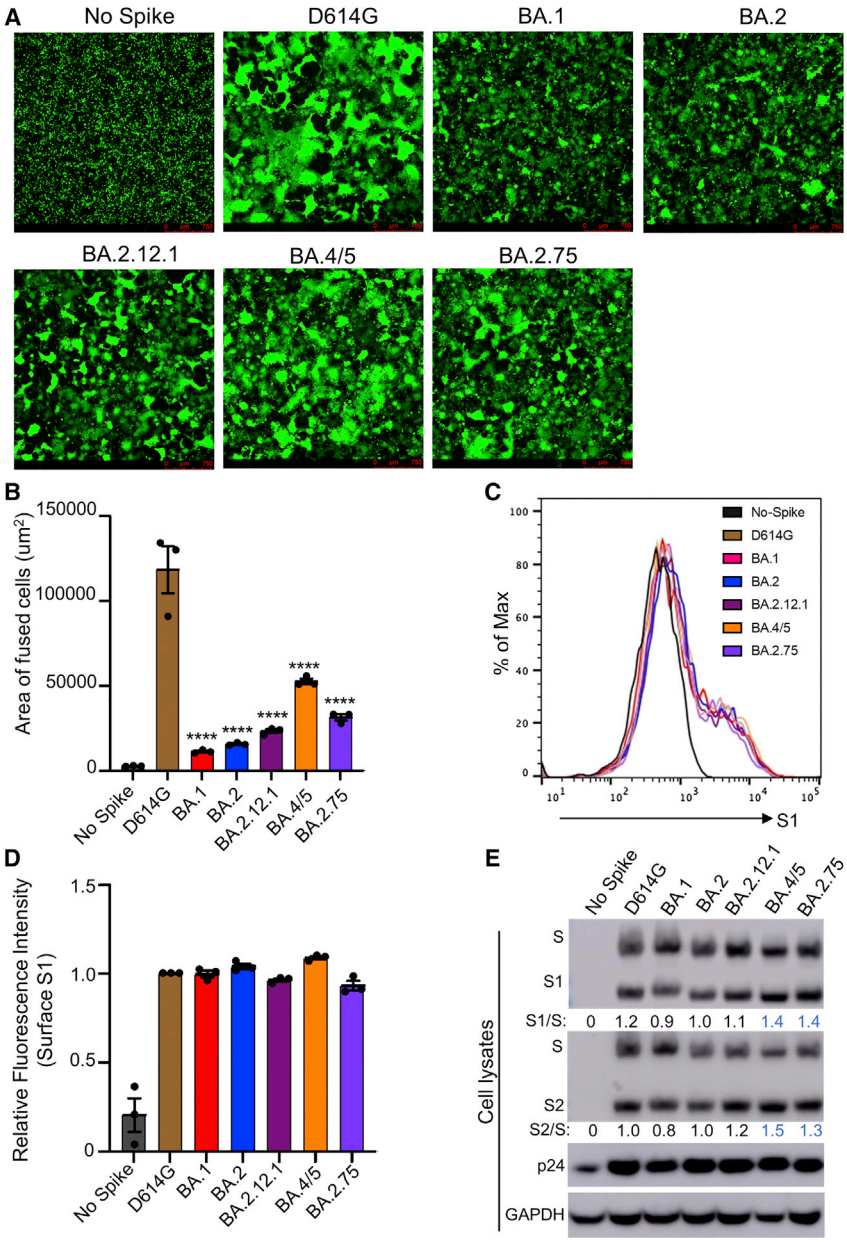

Figure 3. BA.2.75 exhibits enhanced cell-cell fusion and S processing

(A) Fluorescence images displaying syncytia formation are presented for HEK293T-ACE2 cells 48 h after co-transfection with a GFP expression construct and SARS-CoV-2 variant S proteins. Scale bars represent 150 μm.

(B) Quantification of syncytia formation in (A) displays the mean syncytia size; bars represent mean ± standard error, with significance relative to D614G determined by one-way ANOVA with Bonferroni multiplicity correction. p values are displayed as ****p < 0.0001.

(C) Histogram displays of the surface staining of HEK293T cells expressing S proteins, which were detected by an anti-S1 antibody (T62).

(D) Quantification of relative surface expression as shown in (C); bars represent mean ± standard error.

(E) Pseudotyped lentivirus producer cell lysate was assessed for processing of S by probing with anti-S1 (T62), anti-S2, anti-HIV-1 Gag (anti-p24), and anti-GAPDH (glyceraldehyde-3-phosphate dehydrogenase). Band intensities were quantified in ImageJ and the ratio of S1/S or S2/S is displayed relative to the S1/S or S2/S ratio of BA.2.

mutations compared with BA.2, and preliminary reports suggest a slight growth advantage (Callaway, 2022; World Health Organization, 2022). These features portend that BA.2.75 could potentially overtake the BA.4/5 subvariants as the dominant circulating strain. Given this concern, it is critical to examine key features and novel phenotypes of BA.2.75, especially in its S protein. In this study, we show that BA.2.75 exhibits an increased neutralization resistance compared to ancestral BA.2 but has significantly lower neutralization resistance than BA.4/5 for 3-dose mRNA-vaccinated HCWs as well as for hospitalized Omicron-wave patients. Critically, we demonstrate that the G446S and N460K mutations in the S protein of BA.2.75 underlie its enhanced neutralization resistance, while the R493Q mutation in BA.2.75, which is a reversion mutation, sensitizes it to neutralization. These findings could reflect the emergence of compensatory mutations to improve S function while maintaining neutralization resistance. Notably, the G446S mutation occurs in an epitope bound by class III neutralizing antibodies, rather than class II neutralizing antibodies that target the epitope of the R493Q mutation (Greaney et al., 2021). Structural analysis suggests that the side chain addition by G446S creates a steric clash with the CDR region of class III neutralizing antibodies, thus potentially hampering their recognition (Liu et al., 2022; Wang et al., 2022a). Hence, the exchange of these mutations may alter the susceptibility of BA.2.75 to class II and class III nAbs.

We further demonstrate that BA.2.75 exhibits enhanced S-mediated cell-cell fusion compared to BA.2, albeit to a lesser extent than BA.4/5. This enhanced triggering of BA.2.75 S-mediated fusion may reflect improved receptor utilization that is not present in earlier Omicron subvariants, consistent with several recent preprints (Cao et al., 2022; Saito et al., 2022; Wang et al., 2022a). Critically, we find that the N460K mutation present in BA.2.75 is essential for the enhanced fusion phenotype. This may relate to enhanced processing of N460K-containing S in virus producing cells, which would prime more cell surface-associated S for membrane fusion. While structural modeling did not provide an immediate explanation, the N460K mutation might enhance receptor utilization through a hydrogen bond with a receptor glycan N90, and/or through stabilization of the receptor binding motif (RBM) by enhancing intra-domain hydrophilic interactions with D240 and T415 residues. It is worth noting that this glycan interaction is mediated by a terminal mannose molecule, so it may not be easily observed in

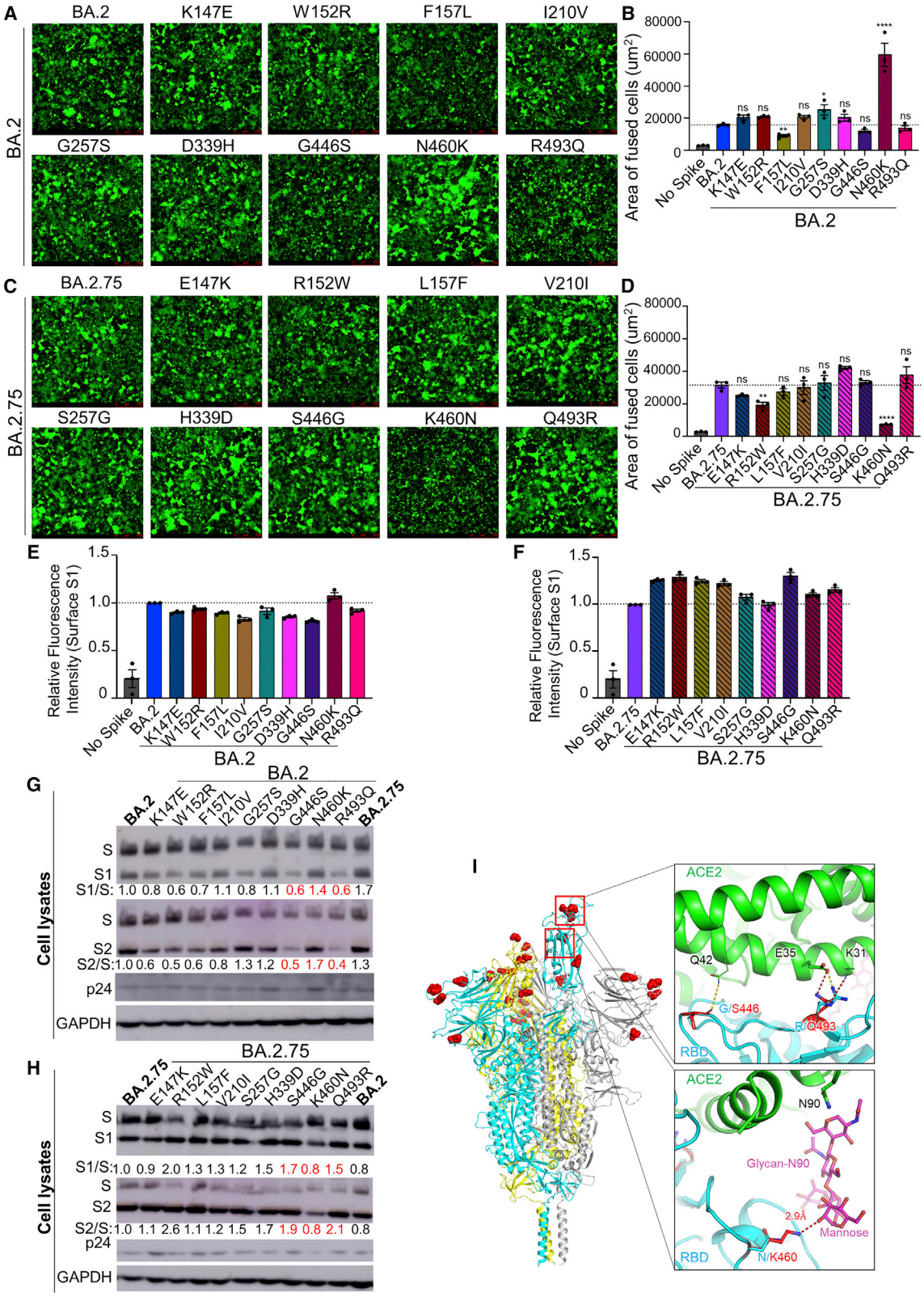

Figure 4. The N460K mutation determines enhanced cell-cell fusion and S processing of BA.2.75

(A) Fluorescence images displaying syncytia formation are presented for HEK293T-ACE2 cells 48 h after co-transfection with a GFP expression construct and BA.2 single mutant S proteins. Scale bars represent 150 μm.

(legend continued on next page)

conditions of protein overexpression where glycosylation is often insufficient, and in cryo-EM where glycan moieties are often less visible. In addition, ACE2 N90-glycan has been shown to be critical for Omicron BA.2 receptor recognition by interacting with RBD residue T415 by crystal structure (Li et al., 2022). The proximity of N460K, D240, T415 and ACE2 N90-glycan enables a strong hydrophilic interaction network to stabilize local conformation and RBD-receptor interactions. G446S, on the other hand, may reduce the flexibility of loop 440–450, potentially enhancing overall spike thermostability, which likely decreases S processing efficiency. Furthermore, G446 is not well resolved in many apo spike structures, in line with its flexible local conformation. A more stable backbone loop conformation produced by the G446S mutation may reduce the energy cost for receptor engagement through hydrogen bond formation with Q42. Lastly, the loss of a strong salt bridge interaction by the R493Q mutation is offset by the addition of two potential hydrogen bonds to the adjacent receptor residues, which could explain its modestly decreased fusion efficiency and processing. The contributions of these key residues to BA.2.75 replication kinetics in physiologically relevant human lung and airway epithelial cells needs to be carefully investigated. Further characterization of emerging SARS-CoV-2 variants will continue to aid our understanding of key features of SARS-CoV-2 evolution, spike biology, and immune evasion. Continued analysis of emerging variants also will improve ongoing public health responses and any potential reformulation of SARS-CoV-2 mRNA vaccine boosters.

Limitations of this study include a relatively small sample size for the boosted HCWs and Omicron-wave patients and the utilization of pseudotyped lentivirus for the neutralization assay rather than an authentic virus assay. However, our results for neutralization resistance are in accordance with several recent preprints (Cao et al., 2022; Gruell et al., 2022; Saito et al., 2022; Sheward et al., 2022; Wang et al., 2022b; Xie et al., 2022; Yamasoba et al., 2022a) and the lentiviral pseudotyped neutralization assay has been previously confirmed using authentic SARS-CoV-2 (Zeng et al., 2020), as well as confirmed by numerous laboratories in the field. Further, the HCWs exhibited a wide range in time between booster administration and sample collection. Additionally, our study hasn't examined the neutralization resistance of BA.2.75 to the nAbs induced by the new bivalent boosters, which have recently received an emergency use authorization (EUA) from the U.S. Food and Drug Administration. It is important to emphasize that while structural modeling is useful and may provide possible explanations to the observations from functional analyses, it is not as accurate as experimental approaches such as X-ray crystallography and cryo-EM. Further structure-based functional mutagenesis analysis will be necessary to delineate the impact of BA.2.75 mutations. Future studies will focus on the biology and replication characteristics of BA.2.75 using variants isolated from human COVID-19 patients.

STAR★METHODS

Detailed methods are provided in the online version of this paper and include the following:

- KEY RESOURCES TABLE
- RESOURCE AVAILABILITY
  - Lead contact
  - Materials availability
  - Data and code availability
- EXPERIMENTAL MODEL AND SUBJECT DETAILS
  - Patient information
  - Cell lines and maintenance
- METHOD DETAILS
  - Plasmids
  - Pseudotyped lentivirus production and infectivity
  - Lentivirus neutralization assay
  - Spike surface expression
  - Syncytia formation
  - Spike processing and incorporation
  - Homology modeling
  - Quantification and statistical analysis

SUPPLEMENTAL INFORMATION

Supplemental information can be found online at https://doi.org/10.1016/j.chom.2022.09.015.

ACKNOWLEDGMENTS

We thank the NIH AIDS Reagent Program and BEI Resources for providing important reagents for this work and Xue Zou for assistance. We also thank the Clinical Research Center/Center for Clinical Research Management of

(B) Quantification of syncytia formation in (A) displays the mean syncytia size; bars represent mean ± standard error, with significance relative to D614G determined by one-way ANOVA with Bonferroni multiplicity correction with p values displayed as *p < 0.05, **p < 0.01, ****p < 0.0001, and ns for not significant.
(C) Fluorescence images displaying syncytia formation are presented for HEK293T-ACE2 cells 48 h after co-transfection with a GFP expression construct and BA.2.75 single reversion mutant S proteins. Note that the negative control for Figures 4A and 4C corresponds to that shown in Figure 3A, which were from the same experiment. Scale bars represent 150 μm.
(D) Quantification of syncytia formation in (C) displays the mean syncytia size; bars represent mean ± standard error, with significance relative to D614G determined by one-way ANOVA with Bonferroni multiplicity correction with p values displayed as **p < 0.01, ****p < 0.0001, and ns for not significant.
(E and F) Quantification of relative S surface expression in transfected HEK293T cells for BA.2 single mutants (E) or BA.2.75 reversion mutants (F), as examined by flow cytometry; bars represent mean ±standard error.
(G) Pseudotyped lentivirus producer cell lysate was assessed for processing of S from BA.2 single mutants by probing with anti-S1 (T62), anti-S2, anti-HIV-1 p24, and anti-GAPDH. Band intensities were quantified in ImageJ and the ratios of S1/S and S2/S are displayed relative to the S1/S and S2/S ratios of BA.2.
(H) Pseudotyped lentivirus producer cell lysate was assessed for processing of S from BA.2.75 reversion mutants by probing with anti-S1, anti-S2, anti-HIV-1 p24, and anti-GAPDH. Band intensities were quantified in ImageJ and the ratios of S1/S and S2/S are displayed relative to the S1/S and S2/S ratios of BA.2.75.
(I) Structural modeling of Omicron BA.2.75 spike protein viewed as a ribbon. Mutations of BA.2.75 specific mutants are highlighted by red spheres. The RBD of the cyan spike protomer is in an "up" conformation. Upper inset: the mutation G446S reduces the backbone flexibility and possibly stabilizes the hydrogen bond between its carbonyl group and the residue Q42 on ACE2 receptor (green); the mutation R493Q abolishes the salt bridge interaction with the E35 on ACE2 receptor and potentially forms two hydrogen bonds with E35 and K31. Lower inset: the mutation N460K enables formation of a hydrogen bond with the glycan-N90 on ACE2 receptor (green).

The Ohio State University Wexner Medical Center and The Ohio State University College of Medicine in Columbus, Ohio, specifically Francesca Madiai, Dina McGowan, Breona Edwards, Evan Long, and Trina Wemlinger, for logistics, collection, and processing of samples. In addition, we thank Sarah Karow, Madison So, Preston So, Daniela Farkas, and Finny Johns in the clinical trials team of The Ohio State University for sample collection and other supports. This work was supported by a fund provided by an anonymous private donor to OSU. S.-L.L., R.J.G., L.J.S., and E.M.O. were supported by the National Cancer Institute of the NIH under award no. U54CA260582. The content is solely the responsibility of the authors and does not necessarily represent the official views of the National Institutes of Health. J.P.E. was supported by Glenn Barber Fellowship from The Ohio State University College of Veterinary Medicine. R.J.G. was additionally supported by the Robert J. Anthony Fund for Cardiovascular Research and the JB Cardiovascular Research Fund, and L.J.S. was partially supported by NIH R01 HD095881. K.X. was supported by a Path to K award from The Ohio State University Office of Head Start and the Center for Clinical & Translational Science. The content is solely the responsibility of the authors and does not necessarily represent the official views of the university or the Center for Clinical & Translational Science.

AUTHOR CONTRIBUTIONS

S.-L.L. conceived and directed the project. P.Q. performed most of the experiments. J.P.E. assisted in experiments and contributed data processing and analyses. C.C. and R.J.G. provided clinical samples. P.Q., J.P.E., and S.-L.L. wrote the paper. K.X. performed homology modeling. Y.-M.Z., L.J.S., E.M.O., and K.X. provided insightful discussion and revision of the manuscript.

DECLARATION OF INTERESTS

The authors declare no competing interests.

Received: August 14, 2022
Revised: September 18, 2022
Accepted: September 26, 2022
Published: September 28, 2022

REFERENCES

Callaway, E. (2022). Will "Centaurus" be the next global coronavirus variant? Indian cases offers clues. Nature *608*, 462–463. https://doi.org/10.1038/d41586-022-02154-4.

Cao, Y., Song, W., Wang, L., Liu, P., Yue, C., Jian, F., Yu, Y., Yisimayi, A., Wang, P., Wang, Y., et al. (2022). Characterizations enhanced infectivity antibody evasion Omicron BA.2.75. Preprint at bioRxiv. https://doi.org/10.1101/2022.07.18.500332.

Centers for Disease Control and Prevention (2022). COVID data tracker. United States Department of Health and Human Services. https://covid.cdc.gov/covid-data-tracker.

Emsley, P., Lohkamp, B., Scott, W.G., and Cowtan, K. (2010). Features and development of Coot. Acta Crystallogr. D Biol. Crystallogr. *66*, 486–501. https://doi.org/10.1107/S0907444910007493.

Evans, J.P., Zeng, C., Qu, P., Faraone, J., Zheng, Y.M., Carlin, C., Bednash, J.S., Zhou, T., Lozanski, G., Mallampalli, R., et al. (2022). Neutralization of SARS-CoV-2 Omicron sub-lineages BA.1, BA.1.1, and BA.2. Cell Host Microbe *30*. 1093.e3–1102.e3. https://doi.org/10.1016/j.chom.2022.04.014.

Goerke, A.R., Loening, A.M., Gambhir, S.S., and Swartz, J.R. (2008). Cell-free metabolic engineering promotes high-level production of bioactive Gaussia princeps luciferase. Metab. Eng. *10*, 187–200. https://doi.org/10.1016/j.ymben.2008.04.001.

Greaney, A.J., Starr, T.N., Barnes, C.O., Weisblum, Y., Schmidt, F., Caskey, M., Gaebler, C., Cho, A., Agudelo, M., Finkin, S., et al. (2021). Mapping mutations to the SARS-CoV-2 RBD that escape binding by different classes of antibodies. Nat. Commun. *12*, 4196. https://doi.org/10.1038/s41467-021-24435-8.

Gruell, H., Vanshylla, K., Tober-Lau, P., Hillus, D., Schommers, P., Lehmann, C., Kurth, F., Sander, L.E., and Klein, F. (2022). mRNA booster immunization elicits potent neutralizing serum activity against the SARS-CoV-2 Omicron variant. Nat. Med. *28*, 477–480. https://doi.org/10.1038/s41591-021-01676-0.

Guex, N., Peitsch, M.C., and Schwede, T. (2009). Automated comparative protein structure modeling with SWISS-MODEL and Swiss-PdbViewer: a historical perspective. Electrophoresis *30*, S162–S173. https://doi.org/10.1002/elps.200900140.

Hoffmann, M., Krüger, N., Schulz, S., Cossmann, A., Rocha, C., Kempf, A., Nehlmeier, I., Graichen, L., Moldenhauer, A.S., Winkler, M.S., et al. (2022). The Omicron variant is highly resistant against antibody-mediated neutralization: implications for control of the COVID-19 pandemic. Cell *185*. 447.e11–456.e11. https://doi.org/10.1016/j.cell.2021.12.032.

Li, L., Liao, H., Meng, Y., Li, W., Han, P., Liu, K., Wang, Q., Li, D., Zhang, Y., Wang, L., et al. (2022). Structural basis of human ACE2 higher binding affinity to currently circulating Omicron SARS-CoV-2 sub-variants BA.2 and BA.1.1. Cell *185*. 2952.e10–2960.e10. https://doi.org/10.1016/j.cell.2022.06.023.

Liu, L., Iketani, S., Guo, Y., Chan, J.F., Wang, M., Liu, L., Luo, Y., Chu, H., Huang, Y., Nair, M.S., et al. (2022). Striking antibody evasion manifested by the Omicron variant of SARS-CoV-2. Nature *602*, 676–681. https://doi.org/10.1038/s41586-021-04388-0.

Mazurov, D., Ilinskaya, A., Heidecker, G., Lloyd, P., and Derse, D. (2010). Quantitative comparison of HTLV-1 and HIV-1 cell-to-cell infection with new replication dependent vectors. PLOS Pathog. *6*, e1000788. https://doi.org/10.1371/journal.ppat.1000788.

Qu, P., Faraone, J., Evans, J.P., Zou, X., Zheng, Y.M., Carlin, C., Bednash, J.S., Lozanski, G., Mallampalli, R.K., Saif, L.J., et al. (2022a). Neutralization of the SARS-CoV-2 Omicron BA.4/5 and BA.2.12.1 subvariants. N. Engl. J. Med. *386*, 2526–2528. https://doi.org/10.1056/NEJMc2206725.

Qu, P., Faraone, J.N., Evans, J.P., Zheng, Y.M., Yu, L., Ma, Q., Carlin, C., Lozanski, G., Saif, L.J., Oltz, E.M., et al. (2022b). Durability of booster mRNA vaccine against SARS-CoV-2 BA.2.12.1, BA.4, and BA.5 subvariants. N. Engl. J. Med. https://doi.org/10.1056/NEJMc2210546.

Saito, A., Tamura, T., Zahradnik, J., Deguchi, S., Tabata, K., Kimura, I., Ito, J., Nasser, H., Toyoda, M., Nagata, K., et al. (2022). Preprint at bioRxiv. https://doi.org/10.1101/2022.08.07.503115.

Schneider, C.A., Rasband, W.S., and Eliceiri, K.W. (2012). NIH Image to ImageJ: 25 years of image analysis. Nat. Methods *9*, 671–675. https://doi.org/10.1038/nmeth.2089.

Sheward, D.J., Kim, C., Fischbach, J., Muschiol, S., Ehling, R.A., Björkström, N.K., Karlsson Hedestam, G.B., Reddy, S.T., Albert, J., Peacock, T.P., and Murrell, B. (2022). Evasion of neutralizing antibodies Omicron sublineage BA.2.75. Preprint at bioRxiv. https://doi.org/10.1101/2022.07.19.500716.

Tuekprakhon, A., Nutalai, R., Dijokaite-Guraliuc, A., Zhou, D., Ginn, H.M., Selvaraj, M., Liu, C., Mentzer, A.J., Supasa, P., Duyvesteyn, H.M.E., et al. (2022). Antibody escape of SARS-CoV-2 Omicron BA.4 and BA.5 from vaccine and BA.1 serum. Cell *185*. 2422.e13–2433.e13. https://doi.org/10.1016/j.cell.2022.06.005.

Wang, Q., Iketani, S., Li, Z., Guo, Y., Yeh, A.Y., Liu, M., Yu, J., Sheng, Z., Huang, Y., Liu, L., and Ho, D.D. (2022a). Antigenic characterization of the SARS-CoV-2 Omicron subvariant BA.2.75. Cell Host Microbe. https://doi.org/10.1016/j.chom.2022.09.002.

Wang, X., Ai, J., Li, X., Zhao, X., Wu, J., Zhang, H., He, X., Zhao, C., Qiao, R., Li, M., et al. (2022b). Preprint at bioRxiv. https://doi.org/10.1101/2022.08.04.502716.

World Health Organization (2022). Tracking SARS-CoV-2 variants. https://www.who.int/en/activities/tracking-SARS-CoV-2-variants.

Xie, X., Zou, J., Liu, M., Ren, P., and Shi, P.Y. (2022). Neutralization of SARS-CoV-2 Omicron sublineages by 4 doses of mRNA vaccine. Preprint at bioRxiv. https://doi.org/10.1101/2022.07.29.502055.

Yamasoba, D., Kimura, I., Kosugi, Y., Uriu, K., Fujita, S., Ito, J., and Sato, K.; The Genotype to Phenotype Japan (G2P-Japan) Consortium (2022a). Preprint at bioRxiv. https://doi.org/10.1101/2022.07.14.500041.

Yamasoba, D., Kimura, I., Nasser, H., Morioka, Y., Nao, N., Ito, J., Uriu, K., Tsuda, M., Zahradnik, J., Shirakawa, K., et al. (2022b). Virological

characteristics of the SARS-CoV-2 Omicron BA.2 spike. Cell *185*. 2103.e19–2115.e19. https://doi.org/10.1016/j.cell.2022.04.035.

Zeng, C., Evans, J.P., Pearson, R., Qu, P., Zheng, Y.M., Robinson, R.T., Hall-Stoodley, L., Yount, J., Pannu, S., Mallampalli, R.K., et al. (2020). Neutralizing antibody against SARS-CoV-2 spike in COVID-19 patients, health care workers, and convalescent plasma donors. JCI Insight *5*, e143213. https://doi.org/10.1172/jci.insight.143213.

Zeng, C., Evans, J.P., Qu, P., Faraone, J., Zheng, Y.M., Carlin, C., Bednash, J.S., Zhou, T., Lozanski, G., Mallampalli, R., et al. (2021). Neutralization and Stability of SARS-CoV-2 Omicron Variant. Preprint at bioRxiv. https://doi.org/10.1101/2021.12.16.472934.

STAR★METHODS

KEY RESOURCES TABLE

REAGENT or RESOURCE	SOURCE	IDENTIFIER
Antibodies		
anti-SARS-CoV-2 S1	Sino Biological	Cat# 40150-T62, RRID:AB_2920715
anti-SARS-CoV-2 S2	Sino Biological	Cat# 40590-T62, RRID: AB_2857932
anti-p24	NIH	Cat# ARP-1513, RRID: AB_2832923
anti-GAPDH	Santa Cruz Biotechnology	Cat# sc-47724, RRID: AB_627678
anti-Rabbit IgG (whole molecule)–FITC antibody	Sigma-Aldrich	Cat# F9887, RRID: AB_259816
anti-Mouse IgG (whole molecule)–Peroxidase	Sigma-Aldrich	Cat# A5278, RRID: AB_258232
anti-Rabbit IgG (whole molecule)–Peroxidase	Sigma-Aldrich	Cat# A9169, RRID: AB_258434
Bacterial and virus strains		
E.coli DH5α	Invitrogen	Strain #: DH5α
E.coli Stable 2	Invitrogen	Strain #: Stable 2
Biological samples		
2-dose HCWs Sera	(Evans et al., 2022; Qu et al., 2022a)	N/A
3-dose HCWs Sera	(Evans et al., 2022; Qu et al., 2022a)	N/A
Omicron-wave Infected Patient Sera	(Evans et al., 2022; Qu et al., 2022a)	N/A
Chemicals, peptides, and recombinant proteins		
Polyethylenimine (PEI)	Thermo Fisher Scientific	Cat# BMS1003
Dulbecco's Modified Eagles Medium (DMEM)	Sigma-Aldrich	Cat#: 11965-092
Fetal Bovine Serum (FBS)	Thermo Fisher Scientific	Cat#: F1051
0.05% Trypsin + 0.53 mM EDTA	Corning	Cat# 25-052-CI
Penicillin-Streptomycin	HyClone	Cat#: SV30010
Protease Inhibitor Cocktail	Sigma-Aldrich	Cat# P8340
Immobilon Crescendo Western HRP substrate	Millipore	Cat# WBLUR0500
QIAprep Spin Miniprep Kit	QIAGEN	Cat# 27106
Coelenterazine	GoldBio	Cat#: CZ2.5, CAS: 55779-48-1
Deposited data		
NT50 Values and De-identified patient data	SeroNet Coordinating Center, NCI, NIH	N/A
Experimental models: Cell lines		
HEK293T	ATCC	Cat#: CRL-11268, RRID: CVCL_1926
HEK293T-ACE2	BEI Resources	Cat#: NR-52511, RRID: CVCL_A7UK
Recombinant DNA		
pNL4-3-inGluc	David Derse, NCI, NIH (Mazurov et al., 2010)	N/A
pcDNA3.1-SARS-CoV-2-Flag-S-Flag_D614G	GenScript Biotech (Evans et al., 2022)	N/A
pcDNA3.1-SARS-CoV-2-Flag-S-Flag_BA.1	GenScript Biotech (Evans et al., 2022)	N/A
pcDNA3.1-SARS-CoV-2-Flag-S-Flag_BA.2.12.1	GenScript Biotech (Qu et al., 2022)	N/A
pcDNA3.1-SARS-CoV-2-Flag-S-Flag_BA.4/5	GenScript Biotech (Qu et al., 2022)	N/A

(*Continued on next page*)

Continued

REAGENT or RESOURCE	SOURCE	IDENTIFIER
pcDNA3.1-SARS-CoV-2-Flag-S-Flag_BA.2.75	GenScript Biotech This paper	N/A
pcDNA3.1-SARS-CoV-2-Flag-S-Flag_BA.2_K147E	This paper	N/A
pcDNA3.1-SARS-CoV-2-Flag-S-Flag_BA.2_W152R	This paper	N/A
pcDNA3.1-SARS-CoV-2-Flag-S-Flag_BA.2_F157L	This paper	N/A
pcDNA3.1-SARS-CoV-2-Flag-S-Flag_BA.2_I210V	This paper	N/A
pcDNA3.1-SARS-CoV-2-Flag-S-Flag_BA.2_G257S	This paper	N/A
pcDNA3.1-SARS-CoV-2-Flag-S-Flag_BA.2_D339H	This paper	N/A
pcDNA3.1-SARS-CoV-2-Flag-S-Flag_BA.2_G446S	This paper	N/A
pcDNA3.1-SARS-CoV-2-Flag-S-Flag_BA.2_N460K	This paper	N/A
pcDNA3.1-SARS-CoV-2-Flag-S-Flag_BA.2_R493Q	This paper	N/A
pcDNA3.1-SARS-CoV-2-Flag-S-Flag_BA.2.75_E147K	This paper	N/A
pcDNA3.1-SARS-CoV-2-Flag-S-Flag_BA.2.75_R152W	This paper	N/A
pcDNA3.1-SARS-CoV-2-Flag-S-Flag_BA.2.75_L157F	This paper	N/A
pcDNA3.1-SARS-CoV-2-Flag-S-Flag_BA.2.75_V210I	This paper	N/A
pcDNA3.1-SARS-CoV-2-Flag-S-Flag_BA.2.75_S257G	This paper	N/A
pcDNA3.1-SARS-CoV-2-Flag-S-Flag_BA.2.75_H339D	This paper	N/A
pcDNA3.1-SARS-CoV-2-Flag-S-Flag_BA.2.75_S446G	This paper	N/A
pcDNA3.1-SARS-CoV-2-Flag-S-Flag_BA.2.75_K460N	This paper	N/A
pcDNA3.1-SARS-CoV-2-Flag-S-Flag_BA.2.75_Q493R	This paper	N/A
pcDNA3.1-SARS-CoV-2-Flag-S-Flag_BA.2	GenScript Biotech (Evans et al., 2022)	N/A
Software and algorithms		
GraphPad Prism	Version 9.0.0	GraphPad
ImageJ	(Schneider et al., 2012)	https://imagej.nih.gov/ij/
FlowJo	FlowJo, LLC	https://www.flowjo.com/
SWISS-MODEL	(Guex et al., 2009)	https://swissmodel.expasy.org/
programs Coot	(Emsley et al., 2010)	https://www2.mrc-lmb.cam.ac.uk/personal/ pemsley/coot/
PyMOL	Warren DeLano and Sarin Bromberg	https://pymol.org/
Leica Application Suite X	Leica Microsystems	https://www.leica-microsystems.com/products/microscope-software/p/leica-las-x-ls/
Other		
Cytation 5 Imaging Reader	BioTek	N/A
L-70 Optima Ultracentrafuge	Beckman	N/A
Amersham Imager 600	GE Healthcare Life Sciences	N/A

RESOURCE AVAILABILITY

Lead contact

Further information and requests for resources and reagents should be directed to the lead contact, Dr. Shan-Lu Liu (liu.6244@osu.edu).

Materials availability

Plasmids generated in this study are available upon request made to the lead contact.

Data and code availability

- NT_{50} values and de-identified patient information will be deposited to the National Cancer Institute SeroNet Coordinating Center. Additionally, NT_{50} values and de-identified patient information reported in this paper will be shared by the lead contact upon request.

- This paper does not report original code.
- Any additional information required to reanalyze the data reported in this paper is available from the lead contact upon request.

EXPERIMENTAL MODEL AND SUBJECT DETAILS

Patient information

Sera were collected from the Ohio State University Wexner Medical Center health care workers (HCWs) under approved institutional review board (IRB) protocols (2020H0228 and 2020H0527). Demographic information was self-reported and all subjects provided informed consent. Sera from 15 HCWs were collected 3-4 weeks after vaccination with a second dose of Moderna mRNA-1273 (n = 7) or Pfizer/BioNTech BNT162b2 (n = 8) vaccine, and 1-12 weeks after vaccination with a homologous booster dose; the relative long duration of sample collection for the booster could contribute to bigger variability in NT_{50} titer. These HCWs ranged in age from 32 to 56 years (median 37 years) and included 6 female and 9 male HCWs. Analysis by age and gender could not be performed due to low sample number.

Sera were collected from patients 30 hospitalized for COVID-19 at the Ohio State University Wexner Medical Center under an approved IRB protocol (2020H0527). Sera were collected between early February and early March of 2022, during the Omicron wave (BA.1 was circulating) in Ohio. Patients included 14 unvaccinated patients, 8 patients vaccinated with 2 doses of Moderna mRNA-1273 (n = 4) or Pfizer/BioNTech BNT162b2 (n = 4), and 8 patients vaccinated and boosted with Pfizer/BioNTech BNT162b2. This cohort included 11 female and 19 male patients. Patients ranged in age from 28 to 78 years (median 62 years).

Cell lines and maintenance

HEK293T (ATCC CRL-11268, RRID: CVCL_1926) and HEK293T-ACE2 (BEI NR-52511, RRID: CVCL_A7UK) cells were maintained in Dulbecco's Modified Eagle's Medium (DMEM) (Cibco, 11965-092) supplemented with 10% Fetal Bovine Serum (Signa, F1051) and 1% penicillin/streptomycin (HyCline, SV30010). Cells were maintained at 5% CO_2 and 37°C.

METHOD DETAILS

Plasmids

Pseudotyped lentivirus was produced using a pNL4-3-inGluc lentivirus vector comprised of a ΔEnv HIV-1 backbone bearing a *Gaussia* luciferase reporter gene driven by a cytomegalovirus (CMV) promoter (Goerke et al., 2008; Zeng et al., 2020). SARS-CoV-2 S constructs bearing N- and C-terminal Flag tags were synthesized and cloned into a pcDNA3.1 vector by GenScript (Piscataway, NJ) by Kpn I and BamH I restriction enzyme cloning.

Pseudotyped lentivirus production and infectivity

Pseudotyped lentivirus was produced by transfecting HEK293T cells with pNL4-3-inGluc and S construct in a 2:1 ratio using polyethylenimine transfection. Pseudotyped lentivirus was collected at 48 hr and 72 hr after transfection. Collections were pooled and used to infect HEK293T-ACE2 cells to assess pseudotyped lentivirus infectivity. 48 hr and 72 hr after infection, infected cell culture media was assessed for *Gaussia* luciferase activity by combining 20 μL of media with 20 μL of *Gaussia* luciferase substrate (0.1 M Tris pH 7.4, 0.3 M sodium ascorbate, 10 μM coelenterazine). Luminescence was then immediately measured by a BioTek Cytation5 plate reader using BioTek Gen5 Microplate Reader and Imager Software (Winooski, VT).

Lentivirus neutralization assay

Pseudotyped lentivirus neutralization assays were performed as previously described (Zeng et al., 2020). Patient or HCW sera were 4-fold serially diluted in complete DMEM and pseudotyped lentivirus was added to neutralize for 1 hr (final dilutions: 1:80, 1:320, 1:1280, 1:5120, 1:20480, and no serum control). The pseudotyped lentivirus/sera mixtures were then transferred to HEK293T-ACE2 cells for infection. Then 48 hr and 72 hr after infection, infected cell media was assayed for *Gaussia* luciferase activity by combining 20 μL of cell culture media with 20 μL of *Gaussia* luciferase substrate. Luminescence was read immediately by a BioTek Cytation5 plate reader using BioTek Gen5 Microplate Reader and Imager Software (Winooski, VT). NT_{50} values were determined by least-squares-fit, non-linear regression in GraphPad Prism 9 (San Diego, CA).

Spike surface expression

HEK293T cells used to produce pseudotyped lentivirus were singularized by incubation in phosphate buffer saline (PBS) with 5 mM ethylenediaminetetraacetic acid (EDTA) at 37°C for 5 min and fixed 72 hr after transfection by incubation in 3.7% formaldehyde in PBS for 10 min. Cells were then stained with rabbit anti-S1 primary antibody (Sino Biological, 40150-T62) and anti-rabbit-IgG-fluorescein isothiocyanate (FITC) secondary antibody (Sigma, F9887). Samples were analyzed by a Life Technologies Attune NxT flow cytometer and data was processed using FlowJo v7.6.5 (Ashland, OR).

Syncytia formation

HEK293T-ACE2 cells were transfected with SARS-CoV-2 S constructs and a GFP expression construct. Cells were then imaged at 4x magnification 24 hr and 48 hr after transfection with a Leica DMi8 confocal microscope. Syncytia size was quantified using Leica Applications Suit X (Wetzlar, Germany) image analysis software. Three images were taken per sample with representative images being displayed.

Spike processing and incorporation

Pseudotyped lentivirus producing HEK293T cells were lysed by incubating in RIPA lysis buffer (50 mM Tris pH 7.5, 150 mM NaCl, 1mM EDTA, Nonidet P-40, 0.1% sodium dodecyl sulfate (SDS)) supplemented with protease inhibitor (Sigma, P8340) on ice for 30 min. Cell debris was pelleted and cell lysate was dissolved in 5x sodium dodecyl-sulfate polyacrylamide gel electrophoresis (SDS-PAGE) Laemmli buffer (312.5 mM Tris-HCl pH 6.8, 10% SDS, 25% glycerol, 0.5% bromophenol blue, 10% β-mercaptoethanol). Pseudotyped lentivirus was purified by ultracentrifugation through a 20% sucrose cushion at 28,000 rpm and 4°C using a Beckman L-80 ultracentrifuge with TW-41 rotor. Pelleted pseudotyped lentivirus was resuspended in 1x SDS-PAGE Laemmli buffer. Cell lysate and purified virus were run on a 10% acrylamide SDS-PAGE gel and were transferred to a polyvinylidene difluorid (PVDF) membrane. Membranes were blotted with anti-S1 (Sino Biological, 40150-T62), anti-S2 (Sino Biological, 40590-T62), anti-p24 (NIH ARP-1513), and anti-glyceraldehyde-3-phosphate dehydrogenase (GAPDH) (Santa Cruz Biotech, sc-47724) with anti-mouse-IgG-horse radish peroxidase (HRP) (Sigma A5278) and anti-rabbit-IgG-HRP (Sigma, A9169) secondary antibodies. Blots were imaged with Immobilon Crescendo Western HRP substrate (Millipore, WBLUR0500) on a GE Amersham Imager 600. Band intensities were quantified using ImageJ (Bethesda, MD) image analysis software.

Homology modeling

Structural modeling of Omicron BA.2.75 spike ectodomain by itself, ectodomain, or RBD in complexes with ACE2 receptor was conducted on SWISS-MODEL server using cryo-EM structures of SARS-CoV2 Omicron BA.1 strain spike ectodomain and ACE2 complex, as well as Omicron BA.2 strain spike RBD in complex with ACE2 (PDB 7TNW, 7TO4 and 7XB0, respectively) as templates. Glycan model building, residue examination, and rotamer adjustment were carried out manually with programs Coot (Emsley et al., 2010) and PyMOL (pymol.org).

Quantification and statistical analysis

NT_{50} values were determined by least-squares-fit, non-linear-regression in GraphPad Prism 9 (San Diego, CA). NT_{50} values were $\log_{10}$ transformed for hypothesis testing to better approximate normality. Throughout, multiplicity was addressed by the use of Bonferroni corrections. Statistical analyses were performed using GraphPad Prism 9 (San Diego, CA) and are referenced in the figure legends and include one-way ANOVA (Figures 3B, 4B, and 4D), one-way repeated measures ANOVA (Figures 1C–1F, 2C, and 2D), and a paired, two-tailed Student's t test with Welch's correction was used (Figures S1A–S1F). Syncytia sizes were quantified by Leica Applications Suit X (Wetzlar, Germany). Band intensities (Figures 3E, 4G, and 4H) were quantified by ImageJ (Bethesda, MD) image analysis software.